

Chapter 3: Manipulation and detection of ultra-cold atoms

All of the experiments described in this thesis were performed using ultracold clouds of ^{87}Rb . In this Chapter I describe the techniques and interactions that make our experiments possible. This Chapter is not meant to be an extensive survey of atomic physics but rather covers the topics that are most relevant to my experiments. The references I included are helpful if the reader is interested in learning the details of the derivations or wants to expand on a given topic. I start by describing the electronic structure of ^{87}Rb . Then I review the interactions of atoms with magnetic fields and its application to magnetic trapping. I describe the foundations of atom-light interactions that make possible both laser cooling and trapping of atoms and give rise to Raman induced transitions. Finally I discuss coherent processes that use the magnetic and electric dipole interaction and are relevant to the experiments presented in Chapters 5, 6 and 8. Finally, I discuss resonant absorption imaging which is used to detect atoms after all our experiments are performed.

3.1 Electronic structure of ^{87}Rb

Rb is an Alkali metal (also Li, which exists in our vacuum chamber but was never used). Alkali metals correspond to the first group (leftmost column) of the periodic table and are characterized by having a single valence electron, which makes the description of their internal structure much simpler than that of other elements. We can describe the state of an electron in an atom by its angular momentum $\hat{\mathbf{L}}$ and its spin $\hat{\mathbf{S}}$. Because of Pauli's exclusion principle there can not be two electrons with the same quantum numbers and in multi-electron atoms they tend to fill 'shells' of different angular momentum values, historically labeled by the letters S , P , D , F , ...¹ (corresponding to $L = 1, 2, 3, 4, \dots$). In particular Rb has 4 filled shells and one electron in the $5S$ shell, where the number 5 corresponds to the principal quantum number n . Figure 1 shows the energy levels of the ground state $5S$ and its closest $5P$ orbital.

The atomic level structure is modified by relativistic effects. In particular the relativistic treatment of the electron's motion gives rise to an interaction between the electron's intrinsic magnetic moment (the spin) $\hat{\mathbf{S}}$ and the orbital angular momentum $\hat{\mathbf{L}}$. This spin-orbit coupling interaction $\hat{H}_{\text{fs}} = A_{\text{fs}} \mathbf{L} \cdot \mathbf{S}$ causes the fine structure splitting of the electronic orbitals into levels with different total electronic angular

¹This terms were used to describe the lines in the emission spectra when they were first discovered. S stands for sharp, P for principal D for diffuse and F for further noted

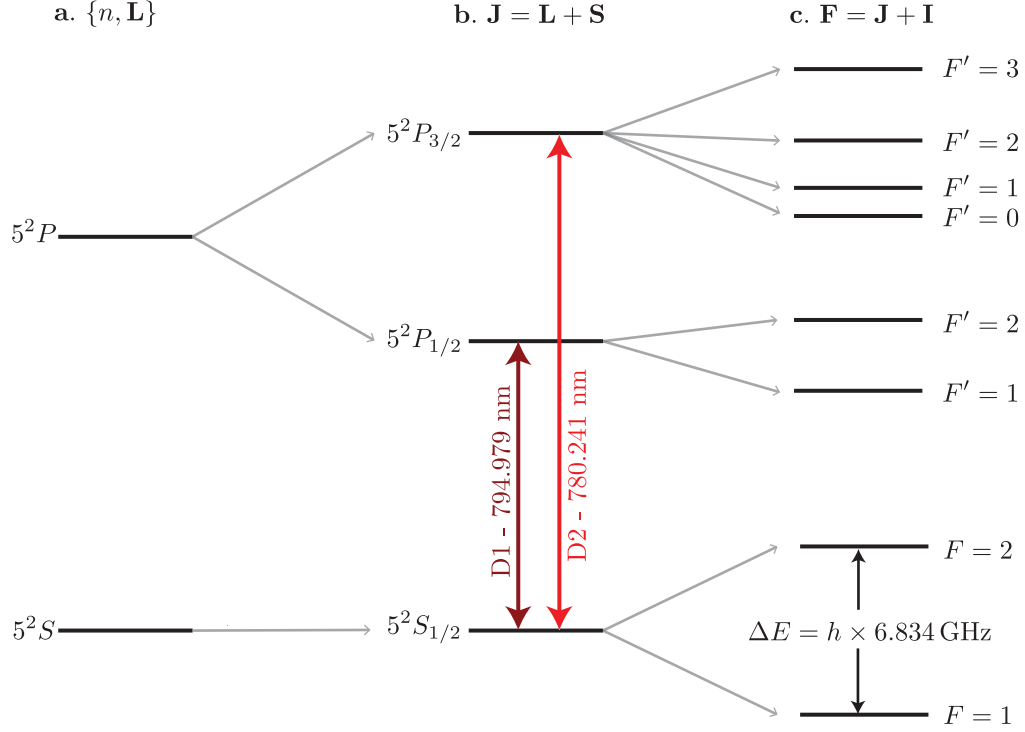


Figure 1: ^{87}Rb level structure (not to scale). **a.** Ground and first excited state electronic configuration of ^{87}Rb given by the $\{n, \mathbf{L}\}$ quantum numbers. **b.** The interaction between the orbital angular momentum and the spin of the electron leads to the fine splitting of orbitals with $L > 0$. The splitting of the 5^2P line gives rise to the D1 and D2 lines. **c.** The interaction between the total angular momentum and the nuclear spin causes the fine structure levels to split further into states characterized by the quantum number F .

momentum $\hat{\mathbf{J}} = \hat{\mathbf{L}} \cdot \hat{\mathbf{S}}$. Figure 1b show the $5^2S_{1/2}$, $5^2P_{1/2}$ and $5^2P_{3/2}$ electronic configurations that arise from this splitting, where the subscript indicates the value of J . For S ($L = 0$) orbitals $J = 1/2$ is the only possible value and the levels are not split. For the P orbital ($L = 1$) J and a single electron with $S = 1/2$, J can be $1/2$ or $3/2$ and the P orbital splits into two levels. The $5^2S_{1/2} \rightarrow 5^2P_{1/2}$ is known as the D1 line and has wavelength $\lambda = 794.979 \text{ nm}$ and $5^2S_{1/2} \rightarrow 5^2P_{3/2}$ transition is known as the D2 line and has $\lambda = 790.241 \text{ nm}$ [1].

The atomic level structure gets further modified by the magnetic interaction of the electron with the nuclear spin \mathbf{I} . This is another kind of spin-orbit interaction that gives rise to the hyperfine splitting of the atomic levels which can be described by the Hamiltonian $\hat{H}_{\text{hfs}} = A_{\text{hfs}} \mathbf{I} \cdot \mathbf{J}$. A complete derivation of \hat{H}_{hfs} can be found in [2]. The hyperfine levels correspond to different values of the total angular momentum $\hat{\mathbf{F}} = \hat{\mathbf{J}} + \hat{\mathbf{I}}$. For ^{87}Rb $I = 3/2$ [1] which results in the level structure shown in Figure 1c.

3.2 Interaction between atoms and magnetic fields

Atoms have an intrinsic magnetic moment that is given by the sum of nuclear and electronic moments

$$\hat{\boldsymbol{\mu}} = -\frac{\mu_B}{\hbar}(g_S\hat{\mathbf{S}} + g_L\hat{\mathbf{L}} + g_I\hat{\mathbf{I}}) \quad (3.1)$$

where μ_B is the Bohr magneton and g_S , g_L and g_I are the Landé ‘ g -factors’ corresponding to the spin, orbital and nuclear angular momentum. In the presence of an external magnetic field \mathbf{B} , the internal levels of an atom get modified due to the Zeeman [3] interaction

$$\hat{H}_{\text{Zeeman}} = -\hat{\boldsymbol{\mu}} \cdot \mathbf{B}. \quad (3.2)$$

If the energy shift due to the Zeeman interaction is small compared to the hyperfine splitting so that F is a good quantum number we can write

$$\hat{H}_{\text{Zeeman}} = \frac{\mu_B g_F}{\hbar} \hat{\mathbf{F}} \cdot \mathbf{B} \quad (3.3)$$

where the hyperfine Landé g -factor is

$$g_F = g_J \frac{F(F+1) - I(I+1) + J(J+1)}{2F(F+1)} + g_I \frac{F(F+1) + I(I+1) - J(J+1)}{2F(F+1)} \quad (3.4)$$

and

$$g_J \approx 1 + \frac{J(J+1) + S(S+1) - L(L+1)}{2J(J+1)}. \quad (3.5)$$

The total energy shifts can be calculated by diagonalizing the full atomic Hamiltonian including the fine and hyperfine structure terms. Figure 2 shows the energies of the m_F levels in the $F = 1$ and $F = 2$ manifolds of ^{87}Rb as a function of magnetic field. If the magnetic field is small then the Zeeman term can be treated as a perturbation to the atomic Hamiltonian and the energy split is linear with the magnitude of the field $E_{m_F} = g_F \mu_B m_F B$, what is known as the ‘linear Zeeman regime’ where F and m_F are good quantum numbers. In contrast, in the ‘Pachet-Back regime’ at large magnetic fields² the Zeeman term dominates over the fine and hyperfine terms and therefore the good quantum numbers of the system are J and m_J . Our experiments typically operate in an intermediate regime ($B \sim 10 - 30$ G, the gray box in Figure 2) where the energy of $m_F = 0$ gets a small shift in energy that is quadratic in B . For atoms in $F = 1$ we define this quadratic Zeeman shift as $\epsilon = E_0 - (E_{+1} - E_{-1})/2$, where E_{m_F} is the Zeeman shift for state m_F .

For the particular case of $J = 1/2$ (like the ground state of Alkalies) the Zeeman energies can be found analytically using the Breit-Rabi formula [4]

$$E_{m_F} = -\frac{1}{2(2I+1)} + \frac{\mu_B g_I m_F B}{\Delta E_{\text{hf}}} + \frac{1}{2} \sqrt{1 + \frac{4m_F}{2I+1}x + x^2}, \quad (3.6)$$

²A couple orders of magnitude larger than the fields we operate at.

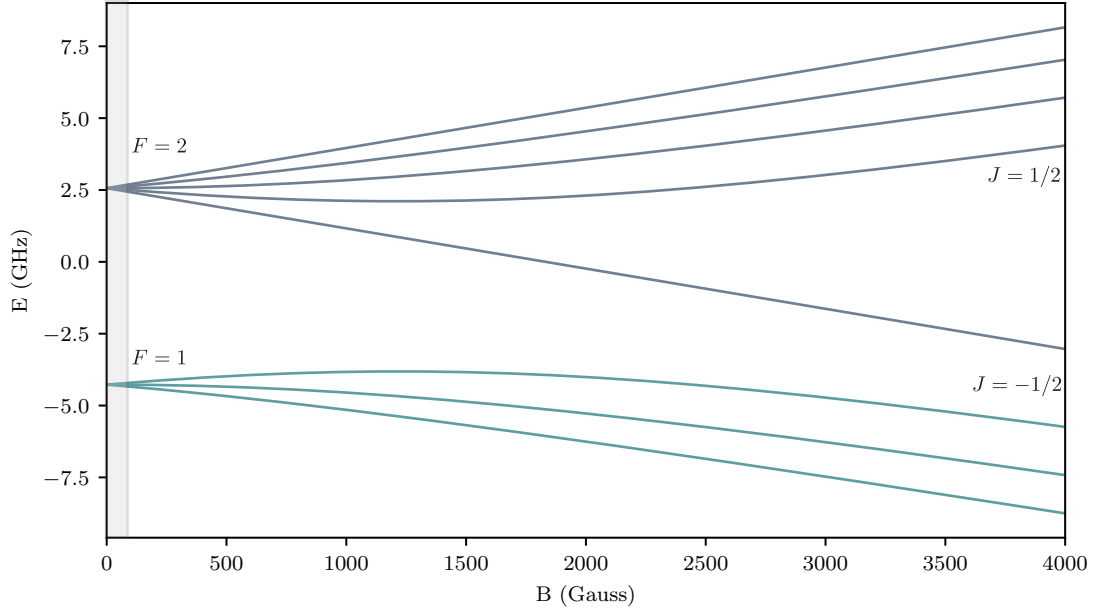


Figure 2: Zeeman splitting of the $5^2S_{1/2}$ manifold of ^{87}Rb . At small magnetic fields F and m_F are good quantum numbers describing the system and at large magnetic fields (Paschen-Back regime) the states are described by the J and m_J . Our experiments operate in the regime marked by the small gray box ($B < 35$ G).

where $\Delta E_{\text{hf}} = A_{\text{hf}}(J + 1/2)$ and $x = (g_J - g_I)\mu_B B_z / \Delta E_{\text{hf}}$. Figure 2 shows the energies of the m_F levels for the $F = 1$ and $F = 2$ manifolds of ^{87}Rb .

3.2.1 Magnetic trapping

The sign of the Zeeman energy for different m_F state can be used to create state dependent traps for atoms. In the lab we implement magnetic traps using quadrupole magnetic fields produced by a pair of anti-Helmholtz coils. The magnetic field near the center of the coils can be written as

$$\mathbf{B} = B'(x\mathbf{e}_x + y\mathbf{e}_y - 2z\mathbf{e}_z) + \mathbf{B}_0 \quad (3.7)$$

where \mathbf{B}_0 is a constant magnetic field, for simplicity I will assume that $\mathbf{B}_0 = B_0\mathbf{e}_z$. The Zeeman Hamiltonian gives a trapping potential

$$\begin{aligned} U(\mathbf{r}) &= g_F\mu_B m_F B' \sqrt{x^2 + y^2 + 4\left(z - \frac{B_0}{2B'}\right)^2} \\ &\approx g_F\mu_B m_F B' \left(\rho + 2\left|z - \frac{B_0}{2B'}\right|\right) \end{aligned} \quad (3.8)$$

where $\rho^2 = x^2 + y^2$ and the approximation on the second line is valid for small displacements from the trap center.

The sign of the magnetic moment determines which states can be trapped. For ^{87}Rb the $|F=1, m_F=-1\rangle$, $|F=2, m_F=2, 1\rangle$ are magnetically trappable.

3.3 Interaction between atoms and electric fields

In this section I will discuss the interaction between atoms and electric fields. After laying the foundations I will discuss applications using off-resonant electromagnetic radiation such as optical dipole traps and Raman transitions. I will not cover laser cooling which has been covered extensively in the literature [5, 6] and PhD theses from previous group members [7, 8].

In the presence of an electric field \mathbf{E} an atom can become polarized and therefore its energy levels get modified by the Stark effect [9]. If the electric field is spatially uniform with respect to the atom's size we consider the electric field as a classical object and its effect on the atom can be described by the the Hamiltonian [10]

$$\hat{H}_{\text{dip}} = -\hat{\mathbf{d}} \cdot \mathbf{E}, \quad (3.9)$$

where $\hat{\mathbf{d}} = -e \sum_j \mathbf{r}_j$ is the atomic dipole operator, e is the electron charge and \mathbf{r}_j are the position operators of the atom's electrons relative to the center of mas of the atom. This approximation, known as the dipole approximation, is valid for electromagnetic radiation when the wavelength is much larger than the size of an atom $\lambda \gg r_{\text{atom}}$ [11].

For a coherent electromagnetic field $\mathbf{E}(\omega, t)$ with angular frequency ω , the dipole Hamiltonian can be written in terms of a dynamic polarizability

$$\hat{H}_{\text{dip}} = -\alpha_{\mu\nu}(\omega) E_{\mu}^{(+)} E_{\nu}^{(-)} \quad (3.10)$$

where $\mathbf{E}^{(\pm)}$ are the possitive/negative frequency components of the field. $\alpha_{\mu\nu}(\omega)$ can be found by looking at the (time averaged) shift in the energy of a given state state using second order time-dependent perturbation theory [11, 12]. For the ground state $|g\rangle$ the polarizability takes the form

$$\alpha_{\mu\nu}(\omega) = \sum_j \frac{2\omega_{jg} \langle g | d_{\mu} | e_j \rangle \langle e_j | d_{\nu} | e_j \rangle}{\hbar(\omega_{jg}^2 - \omega^2)}, \quad (3.11)$$

where $|e_j\rangle$ represent the excited states and $\omega_{jg} = (E_j - E_g)/\hbar$. The dipole operator is a rank-2 tensor and can be represented by 3 irreducible tensor operators (see [11] for a complete derivation). In the limit of small magnetic fields so that F and m_F are good quantum numbers describing the state of the atom $|n, F, m_F\rangle$ the dipole

Hamiltonian in this representation takes a convenient form

$$\begin{aligned}\hat{H}_{\text{dip}} = & \alpha^{(0)}(\mathbf{E}^{(-)} \cdot \mathbf{E}^{(+)}) + i\alpha^{(1)}(\mathbf{E}^{(-)} \times \mathbf{E}^{(+)}) \cdot \hat{\mathbf{F}} \\ & + \alpha^{(2)} E_i^{(-)} E_j^{(+)} \left(\frac{1}{2}(F_i F_j + F_j F_i) - \frac{1}{3} \hat{\mathbf{F}}^2 \delta_{ij} \right) \Big],\end{aligned}\quad (3.12)$$

where $\alpha^{(0)}$, $\alpha^{(1)}$ and $\alpha^{(2)}$ are the scalar, vector and tensor polarizabilities respectively and $\hat{\mathbf{F}}$ is the total angular momentum operator. For all our experiments $\alpha^{(2)}$ is very small so I will limit the discussion to the effect of the first two terms. The scalar term is responsible for the dipole force that allow us to trap atoms using off-resonant light and the vector component is necessary for engineering spin-orbit coupling and other spin-dependent potentials through two-photon processes.

3.3.1 Scalar polarizability

The scalar polarizability takes the form

$$\alpha^{(0)} = \sum_j \frac{2\omega_{jg} \langle g | \mathbf{d} \cdot \hat{\mathbf{e}} | e_j \rangle|^2}{\hbar(\omega_{jg}^2 - \omega^2)}, \quad (3.13)$$

where $\hat{\mathbf{e}}$ represents the polarization vector of the light. The matrix element can be expressed in terms of the Clebsch-Gordan coefficients and the reduced matrix element using the Wigner-Eckart theorem [13]. For the ground state of an Alkali atom ($J = 1/2$) and if the detuning is large compared to the hyperfine splitting the expression above gets simplified to

$$\alpha^{(0)} \approx \sum_{J'} \frac{2\omega_{JJ'} |\langle J = 1/2 || \mathbf{d} || J' \rangle|^2}{3\hbar(\omega_{JJ'}^2 - \omega^2)}. \quad (3.14)$$

The dipole matrix elements needed to compute the polarizability are related to the transition scattering rate via Fermi's golden rule [11, 13]

$$\Gamma_{JJ'} = \frac{\omega_{JJ'}^2}{3\pi\epsilon_0\hbar c^3} \frac{2J+1}{2J'+1} |\langle J || \mathbf{d} || J' \rangle|^2, \quad (3.15)$$

and combining this with the expression for the intensity of the electric field $I(\mathbf{r}) = 2\epsilon_0 c |\mathbf{E}(\mathbf{r})|^2$ it can be shown that for linearly polarized light the energy of the ground state manifold is shifted by

$$U(\omega, \mathbf{r}) = -\frac{\pi c^2 I(\mathbf{r})}{2} \left[\frac{\Gamma_{D1}}{\omega_{D1}^3} \left(\frac{1}{\omega + \omega_{D1}} - \frac{1}{\omega - \omega_{D1}} \right) + \frac{2\Gamma_{D2}}{\omega_{D2}^3} \left(\frac{1}{\omega + \omega_{D2}} - \frac{1}{\omega - \omega_{D2}} \right) \right], \quad (3.16)$$

where only the the most significant contribution from the closest transitions (the D1 and D2 lines) are included. Here $U(\mathbf{r})$ is related to the real part of the polarizability which is in fact a complex valued number. So far I have only considered a real valued polarizability by assuming the excited states have an infinitely long lifetime.

However, in reality the atom can spontaneously emit photons and decay. This exponential decay can be accounted for by adding an imaginary contribution to the energies $\omega_D \rightarrow \omega_D + i\Gamma_D\omega^3/\omega_D^3$ of the D1 and D2 transitions [14]. The scattering rate is related to the imaginary part of the polarizability and is given by

$$\Gamma(\omega, \mathbf{r}) = \frac{\pi c^2 I(\mathbf{r})}{2\hbar} \left[\frac{\Gamma_{D1}\omega^3}{\omega_{D1}^6} \left(\frac{1}{\omega + \omega_{D1}} - \frac{1}{\omega - \omega_{D1}} \right)^2 + \frac{2\Gamma_{D2}\omega^3}{\omega_{D2}^6} \left(\frac{1}{\omega + \omega_{D2}} - \frac{1}{\omega - \omega_{D2}} \right)^2 \right] \quad (3.17)$$

The energy shift $U(\omega, \mathbf{r})$ is a conservative term and is related to dipole trapping while the scattering term $\Gamma(\omega, \mathbf{r})$ is dissipative and is important for laser cooling. In the context of engineering potentials for ultracold atoms with off-resonant light, the scattering is translated into heating because every time an atom emits a photon with angular frequency ω_L it gets a recoil momentum $\hbar\mathbf{k}_L$. If the frequency ω satisfies the relation $\omega + \omega_D \gg \omega - \omega_D$, as is often the case, we can neglect the terms proportional to $1/(\omega + \omega_D)$, an approximation typically known as the rotating wave approximation (RWA). If the RWA is valid then the frequency dependence of both the energy shifts and the scattering rates will be given by the detuning from the D1 and D2 transitions.

3.3.1.1 Optical trapping

One important application of the scalar light-shift is to create optical traps for clouds of ultracold atoms. An optical field with non-uniform spatial intensity generates traps (and anti-traps) for the atoms which experience a force proportional to the intensity gradient $F_{\text{dip}} = -\nabla U(\mathbf{r})$. The attractive or repulsive nature of the trap depends on the sign of $U(\mathbf{r})$ which is determined by the sign of the detuning (blue-detuned traps are repulsive and red-detuned traps are attractive) [TODO: make nice figure of dipole trap if I have time]. The production of BECs in our lab relies on the use of focused Gaussian laser beams with $\lambda = 1064 \text{ nm}$. The intensity profile of a focused Gaussian beam propagating along \mathbf{e}_z is given by

$$I(x, y, z) = \frac{2P}{\pi\omega^2(z)} e^{-\frac{x^2+y^2}{\omega^2(z)}} \quad (3.18)$$

where P is the total power of the beam and the $1/e^2$ radius is given by $w(z) = w_0\sqrt{1 + z^2/z_R^2}$ where the minimum radius w_0 is known as the waist and $z_R = \pi\omega_0^2/\lambda$ is the Rayleigh range. If the extent of an atomic cloud is small compared to the size of the beam we can perform a Taylor expansion around $\mathbf{r} = 0$ to obtain the trapping potential

$$U(\mathbf{r}) = -U_0 \left(1 - 2\frac{x^2 + y^2}{\omega_0^2} - \frac{z^2}{z_R^2} \right). \quad (3.19)$$

The oscillation frequencies of the trap along the radial direction are $\omega_r = (4U_0/m\omega_0^2)^{1/2}$ and along the axial direction $\omega_z = (2U_0/mz_R)^{1/2}$. The beam waist is usually much smaller than the Rayleigh range ($\omega_0 \sim 50 - 150 \text{ nm}$ for my experiments) and therefore the trap is much stronger along the axial direction. To get around this we use

a ‘crossed dipole trap’ which is formed by a combination of two cross-polarized³ focused Gaussian beams propagating along perpendicular axes, ensuring that we get good confinement of atoms along all spatial directions.

3.3.2 Vector polarizability and effective magnetic fields

For Alkali atoms the vector polarizability takes the form [11, 15]

$$\alpha^{(1)} = \frac{2\alpha^{(0)}\Delta_{\text{fs}}}{3(\tilde{E} - \hbar\omega)} \quad (3.20)$$

where $\Delta_{\text{fs}} = 3A_{\text{fs}}/2$ and $\tilde{E} = (2E_{\text{D}_1} + E_{\text{D}_2})$. If we recall the Zeeman Hamiltonian introduced in Section 3.2, the term proportional to the vector polarizability in Equation 3.12 looks very similar to Equation 3.2 for an effective magnetic field

$$\mathbf{B}_{\text{eff}} = -\frac{i\hbar}{\mu_B g_J} \alpha^{(1)} (\mathbf{E}^* \times \mathbf{E}). \quad (3.21)$$

For the intensities that we typically operate at, the vector light shift is small and can be treated as a perturbation. The Hamiltonian resulting from this effective magnetic field can be written as

$$\hat{H}_{\text{eff}} = \frac{\mu_B g_F}{\hbar} \mathbf{B}_{\text{eff}} \cdot \hat{\mathbf{F}} \quad (3.22)$$

3.3.2.1 Raman coupling

The vector light shift enables the realization of various spin dependent potentials in the lab. In the experiments presented in Chapters 5 and 8 I used combinations of cross polarized laser beams such that the total electric field $\mathbf{E}^* \times \mathbf{E} \neq 0$ and we induced two-photon Raman transitions. A Raman transition is a two-photon process between two ground states that uses an intermediate state that is off-resonantly coupled as is shown in Figure 3a. Due to the large detuning, the population transferred into the intermediate state is negligible and the state can be adiabatically eliminated [16]. In our experiments we typically couple the m_F levels of the $F = 1$ manifold after applying a bias magnetic field such that ϵ is non-negligible.

Consider two laser beams counter propagating along \mathbf{e}_x and with polarizations along \mathbf{e}_y and \mathbf{e}_z as is shown in Figure 3b. The electric field from the Raman beams is given by

$$\mathbf{E}(x, t) = E_a \cos(k_a x - \omega_a t) \mathbf{e}_y + E_b \cos(k_b x + \omega_b t) \mathbf{e}_z, \quad (3.23)$$

and consequently

$$\mathbf{E}^* \times \mathbf{E} = 2iE_a E_b \cos(2k_L x - \omega_{a,b} t) \mathbf{e}_x, \quad (3.24)$$

³The beams are cross-polarized to avoid interference between them

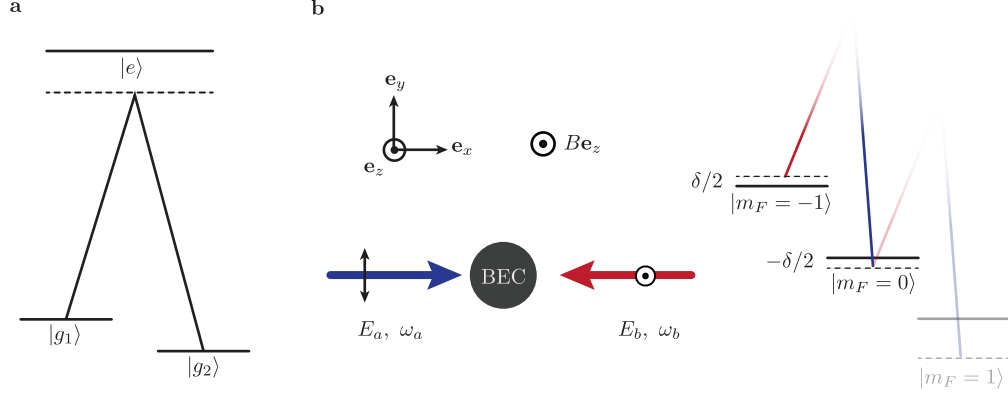


Figure 3: **a.** A Raman transition is a two photon process that couples two ground state through and intermediate far detuned state. **b.** We induce Raman transitions using a pair of cross-polarized laser beams whose and we set the difference in their angular frequencies close to the Zeeman splitting between two consecutive m_F states.

where $\omega_{a,b} = \omega_a - \omega_b$. The Raman Hamiltonian is given by

$$\hat{H}_R = \Omega \cos(2k_L x - \omega_{a,b} t) \hat{F}_x \quad (3.25)$$

where $\Omega = \alpha^{(1)} g_F E_a E_b / g_J \propto \sqrt{I_a I_b}$ is the Raman coupling strength. The geometry and wavelength of the Raman fields determine the natural units of the system: the single photon recoil momentum $k_L = 2\pi/\lambda_R$ and its associated recoil energy $E_L = \hbar^2 k_L^2 / 2m$, as well as the direction of the recoil momentum $\mathbf{k}_L = k_L \mathbf{e}_x$. For most experiments we tune to what is known as the ‘magic wavelength’ or tune-out wavelength [17] $\lambda_R = 790.034$ nm, at which the ground-state scalar polarizability vanishes and the scattering rate is reduced (Figure 4a,c). We occasionally had to tune away from the magic wavelength, for example when we were starving for laser power and wanted to increase our Raman coupling strength; Figure 4b shows the dependence of the Raman coupling strength on wavelength and 4d shows the decay in number of Raman dressed atoms as a function of time for different wavelengths.

In a frame rotating with angular frequency $\omega_{a,b}$ corresponding to applying the unitary transformation $\hat{U}(t) = \exp(-i\omega_{a,b} t \hat{F}_z)$ and neglecting the fast terms rotating at frequency $2\omega_{a,b}$ (applying a RWA) the transformed Hamiltonian is

$$\hat{U}^\dagger \hat{H}_R \hat{U} - i\hbar \hat{U}^\dagger \partial_t \hat{U} = \omega_{a,b} \hat{F}_z + \frac{\Omega}{2} \cos(2k_L x) \hat{F}_x - \frac{\Omega}{2} \sin(2k_L x) \hat{F}_y, \quad (3.26)$$

which describes a helically precessing magnetic field with period $\lambda_R/2$.

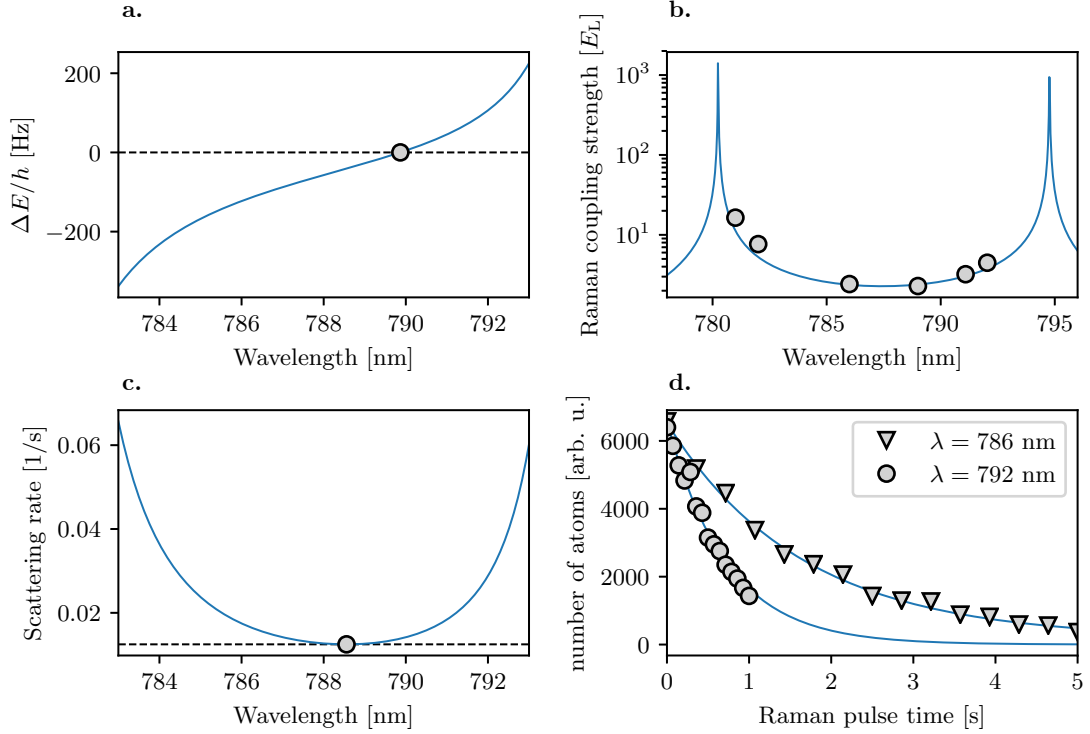


Figure 4: **a.** Scalar polarizability as a function of wavelength near the D1 and D2 lines of ^{87}Rb . We typically tune our Raman laser beams near the magic wavelength $\lambda = 790.034\text{ nm}$. **b.** Raman coupling strength as a function of wavelength measured for a pair of Raman beams with waist $w_0 \sim 150\text{ }\mu\text{m}$ and powers of $50, 10\text{ }\mu\text{W}$. **c.** Scattering rate as a function of wavelength, while it is not minimized at 790 nm its value is kept relatively low. **d.** Decay in number of Raman dressed atoms as a function of hold time for the same beam parameters as in **b.**. At $\lambda = 786\text{ nm}$ the $1/e$ lifetime is $\tau = 1.64\text{ s}$ and for $\lambda = 792\text{ nm}$ it is reduced to $\tau = 0.72\text{ s}$.

3.3.2.2 Spin-orbit coupling

The Raman Hamiltonian from Equation 3.26 can be massaged a bit more to make it look like a spin-orbit coupled (SOC)⁴ Hamiltonian that is familiar to condensed matter physicists. If we apply a spin-dependent momentum boost which is described by the unitary operator $\hat{U}(k_L) = \exp(i2k_L x \hat{F}_z)$ the full Hamiltonian including the Raman coupling and the free particle energies is transformed to

$$\hat{H}_{\text{SOC}} = \frac{\hbar^2}{2m} (\hat{q}_x - 2k_L \hat{F}_z)^2 + \frac{\Omega}{2} \hat{F}_x + \delta \hat{F}_z + \hbar\epsilon \left(\mathbb{1} - \frac{\hat{F}_z^2}{\hbar^2} \right), \quad (3.27)$$

⁴Not to be confused with the spin-orbit coupling giving rise to the fine and hyperfine structure mentioned earlier, perhaps a better name could be spin-momentum coupling

where $\delta = E_{-1} - \omega_{a,b}$. We can go from a 3 level system to an effective spin-1/2 system if we set $\Delta\omega = E_{-1} - E_0$ and consider a sizable quadratic Zeeman shift ϵ , the $m_F = 1$ state can be adiabatically eliminated [18] and the Hamiltonian becomes

$$\hat{H}_{SOC} = \frac{\hbar^2}{2m}(q_x - k_L \hat{\sigma}_y)^2 + \frac{\hbar}{2}\Omega \hat{\sigma}_z + \frac{\hbar}{2}\delta \hat{\sigma}_y \quad (3.28)$$

where $\sigma_{x,y,z}$ are the Pauli matrices. The Hamiltonian above corresponds to an equal superposition of Rashba-type [19] ($\propto \hat{\sigma}_x k_y - \hat{\sigma}_y k_x$) and Dresselhaus-type [20] ($\propto -\sigma_x k_y - \sigma_y k_x$) SOC with an effective magnetic field $\propto \Omega$ in the $\mathbf{e}_y - \mathbf{e}_z$ plane [18, 21]. In Chapter 8 I discuss the Rashba term in more detail and introduce a way of engineering a system with only Rashba-type SOC using multiple internal levels and Raman transitions.

3.4 Coherent manipulation

In this section I describe quantum coherent processes that are driven using the magnetic and electric dipole interactions described in previous sections. We rely on this techniques both for state preparation and characterization of our system. In all of the cases I consider a system described by the Hamiltonian

$$\hat{H} = \hat{H}_0 + \hat{H}_I(t) \quad (3.29)$$

where \hat{H}_0 describes unperturbed atomic levels and $\hat{H}_I(t)$ is a time dependent interaction. For simplicity I consider only a two-level system

$$\hat{H}_0 = \hbar \begin{pmatrix} \omega_g & 0 \\ 0 & \omega_e \end{pmatrix} \quad (3.30)$$

where with $|g\rangle$ and $|e\rangle$ are the unperturbed ground and excited states with energy $\hbar\omega_i$ are the energies of the unperturbed states.

3.4.1 Rabi oscillations

First I consider an interaction term that oscillates with frequency ω close to the transition energy $\omega_{ge} = \omega_g - \omega_e$

$$\hat{H}_I = \hbar \begin{pmatrix} 0 & \Omega \cos(\omega t) \\ \Omega^* \cos(\omega t) & 0 \end{pmatrix} \quad (3.31)$$

the coupling strength Ω here could be related to an electric dipole transition $\Omega \propto \langle g | \mathbf{d} \cdot \mathbf{E} | e \rangle$ ⁵ or magnetic dipole $\Omega \propto \langle g | \boldsymbol{\mu} \cdot \mathbf{B} | e \rangle$ transition matrix element. The

⁵For our system intensities $\Gamma \gg \Omega$ and we don't observe Rabi oscillations from (single photon) electric dipole transitions.

state of the system at any given time is given by

$$|\Psi\rangle = c_g(t)e^{-i\omega_g t} |g\rangle + c_e(t)e^{-i\omega_e t} |e\rangle, \quad (3.32)$$

and substituting this expression into the time dependent Schrödinger equation we find that

$$\begin{aligned} \dot{c}_g(t) &= \frac{\Omega}{2} \left(e^{i(\omega - \omega_{ge})t} + e^{-i(\omega + \omega_{ge})t} \right) c_e \\ \dot{c}_e(t) &= \frac{\Omega^*}{2} \left(e^{i(\omega - \omega_{ge})t} + e^{-i(\omega + \omega_{ge})t} \right) c_g. \end{aligned} \quad (3.33)$$

We can apply a RWA if the term $\omega + \omega_{ge}$ is large compared to $\omega - \omega_{ge}$. The resulting coupled differential equations can be solved in a standard way by differentiating \dot{c}_e one more time and substituting \dot{c}_g . If we assume that at $t = 0$ the system is prepared in $|g\rangle$ the population in $|e\rangle$ describes what is known as a Rabi oscillation [22]

$$|c_e(t)|^2 = \frac{\Omega^2}{\Omega^2 + \delta^2} \sin^2 \left(\frac{\sqrt{\Omega^2 + \delta^2}}{2} t \right) \quad (3.34)$$

where $\delta = \omega - \omega_{ge}$ is a detuning and $\tilde{\Omega} = \sqrt{\Omega^2 + \delta^2}$ is known as the generalized Rabi frequency. The Hamiltonian after applying the RWA can be written as

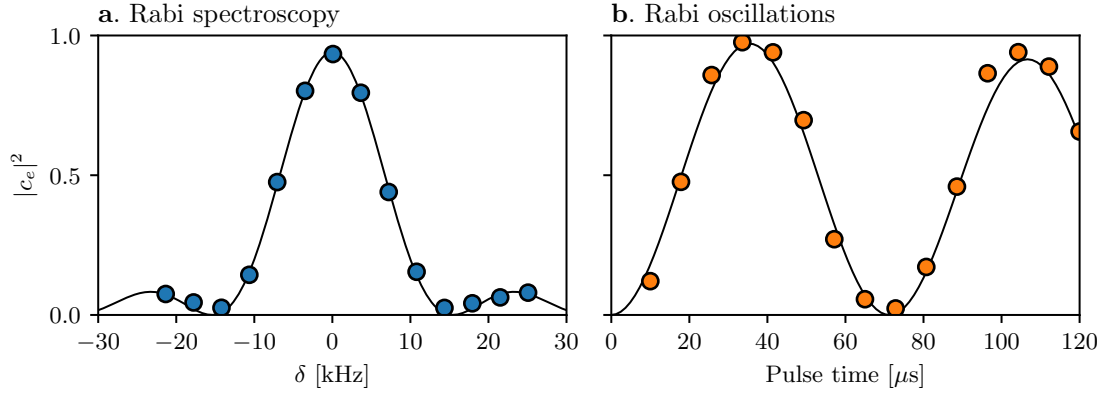


Figure 5: The Rabi cycle. **a.** Population transferred to the excited state as a function of detuning for a $60 \mu\text{s}$ pulse and $\Omega = 7.1 \text{ kHz}$. **b.** Population transferred as a function of time for a $\Omega = 14 \text{ kHz}$ close to resonance.

$$\hat{H}_0 = \hbar \begin{pmatrix} -\delta/2 & \Omega/2 \\ \Omega^*/2 & \delta/2 \end{pmatrix}, \quad (3.35)$$

and its eigenenergies correspond to $E_{\pm} = \pm \tilde{\Omega}/2$. Notice that the difference between the eigenenergies $E_+ - E_-$ is exactly equal to the frequency at which the populations

in $|g, e\rangle$ oscillate, this will come up again in Chapter 5. Figure 5a shows the population in $|e\rangle$ as a function of δ for a π pulse ($\delta = 0, \Omega t = \pi$). The location of the peak in this curve is as a way to find the transition frequency (we use this method in Chapter 6). Figure 5b shows the population transferred into $m_F = 0$ from $m_F = -1$ as a function of time; we typically look at the frequency of these Rabi oscillations to calibrate the coupling strength of an effective two-level system.

3.4.2 Ramsey interferometer

Now I consider a Ramsey interferometer [23], a setup that is relevant to Chapters 6 and 8. The interaction Hamiltonian is the same as in the previous section but rather than being on continuously it is pulsed on for a time $\tau = \pi/2\Omega$ (a $\pi/2$ pulse), then the system is let to evolve only under \hat{H}_0 for a variable time t_{dark} and finally a second $\pi/2$ pulse is applied. Figure 6a illustrates this protocol: the $\pi/2$ pulses can be thought of as $\pi/2$ rotations on the Bloch sphere along \mathbf{e}_x transforming the initial state $|g\rangle \rightarrow (|g\rangle + |e\rangle)/\sqrt{2}$. During the dark time the system precesses on the equator of the Bloch sphere by an angle δt_{dark} and finally the second pulse rotates the state along the \mathbf{e}_x axis again. The probability of measuring the excited state is related to the phase accumulated during the dark time is given by

$$|c_e(2\tau + t_{\text{dark}})|^2 = \left| \frac{\Omega\tau}{2} \right| \left[\frac{\sin(\delta\tau/2)}{\delta\tau/2} \right]^2 \cos^2 \left(\frac{\delta t_{\text{dark}}}{2} \right), \quad (3.36)$$

where the oscillation frequency is only determined by the detuning. In contrast, for a Rabi oscillation the detuning adds in quadrature with Ω , which suppresses the effect of the detuning when it is large as $\tilde{\Omega} \approx \Omega + \delta^2/2\Omega$. This will be important in Chapter 6 and additionally in Chapter 8 I rely on a variation of the Ramsey interferometer to perform quantum state tomography. Figure 6b shows an example of a Ramsey fringe as a function of detuning δ that we measured using two states coupled with $\Omega = 1$ kHz.

3.4.3 Floquet theory

The RWA has been used multiple times throughout this Chapter so that the Hamiltonian describing a driven systems can effectively be viewed as time independent. This approximation is valid most of the time for our experiments, however, if we want to give a complete description of a time periodic system Floquet theory can be helpful. I will give a brief overview of Floquet theory using a matrix approach that is particularly useful for numerical computations.

Consider a time periodic Hamiltonian $\hat{H}(t) = \hat{H}(t+T)$. We can write in terms of its Fourier components

$$\hat{H}(t) = \sum_{j=-\infty}^{\infty} \exp[ij\omega t] \hat{H}_j, \quad (3.37)$$

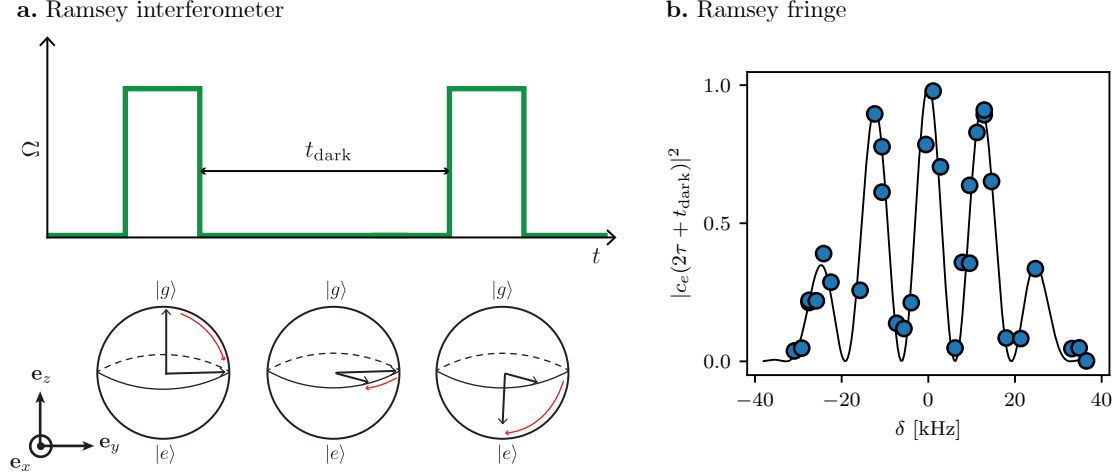


Figure 6: **a.** A Ramsey interferometer: Two $\pi/2$ pulses are separated by a time t_{dark} . The phase accumulated in the interferometer is equal to the detuning multiplied by the dark time. **b.** A Ramsey interference fringe obtained from coupling two levels using an RF field with $\Omega = 1$ kHz. We applied a pair of $\tau = 25 \mu\text{s}$ pulses separated by a $50 \mu\text{s}$ wait and varied the detuning by changing the bias magnetic field.

where $\omega = 2\pi/T$ and because \hat{H} is Hermitian the operators must satisfy $\hat{H}_j = \hat{H}_{-j}^\dagger$. The eigenstates of the Hamiltonian can be written in a terms of quasi periodic functions⁶

$$|\psi_\epsilon(t)\rangle = \exp(-i\epsilon t/\hbar) \sum_{k=-\infty}^{\infty} \exp[-ik\omega t] |\psi_{\epsilon,k}\rangle \quad (3.38)$$

where the term ϵ is known as the quasi-energy. Inserting this expression into the time-dependent Schrödinger equation gives

$$\sum_k (\epsilon + \hbar\omega k) \exp[-k\omega t] |\psi_{\epsilon,k}\rangle = \sum_{j,j'} \exp[i(j-j')\omega t] \hat{H}_{j'} |\psi_{\epsilon,j}\rangle. \quad (3.39)$$

In order for the equality to be true we must have $j' - j = -k$ because the complex exponentials form an orthonormal basis and we can write

$$\epsilon |\psi_{\epsilon,k}\rangle = \sum_j \left(\hat{H}_{j-l} - \hbar\omega k \delta_{j,k} \times \hat{\mathbf{1}} \right), \quad (3.40)$$

⁶Very much like Bloch wave functions

where $\hat{\mathbb{1}}$ is the identity matrix. The expression can be recast into a matrix form

$$\epsilon \begin{pmatrix} \cdots \\ |\psi_{\epsilon,-1}\rangle \\ |\psi_{\epsilon,0}\rangle \\ |\psi_{\epsilon,1}\rangle \\ \cdots \end{pmatrix} = \begin{pmatrix} \hat{H}_0 + 2\hbar\omega & \hat{H}_1 & \hat{H}_2 & \cdots & \cdots \\ \hat{H}_{-1} & \hat{H}_0 + \hbar\omega & \hat{H}_1 & \hat{H}_2 & \cdots \\ \hat{H}_{-2} & \hat{H}_{-1} & \hat{H}_0 & \hat{H}_1 & \cdots \\ \cdots & \hat{H}_{-2} & \hat{H}_{-1} & \hat{H}_0 - \hbar\omega & \hat{H}_1 \\ \cdots & \cdots & \hat{H}_{-2} & \hat{H}_{-1} & \hat{H}_0 - 2\hbar\omega \end{pmatrix} \quad (3.41)$$

The quasienergies ϵ can be computed by truncating and then diagonalizing the matrix, and they are grouped into repeating manifolds separated in energy by $\hbar\omega$. The quasienergies within a manifold can be interpreted as the eigenenergies of an effective time-independent Hamiltonian \hat{H}_{Fl} that describes the evolution of the system sampled stroboscopically at an integer number of driving periods, with the time evolution operator $\hat{U}(t_0, t_0 + T) = e^{-iT\hat{H}_{Fl}}$.

Floquet theory played an important role in the engineering of different dispersion relations for atoms in Chapters 5 and 8. I will give an example based on [24], where we considered a pair of Raman beams driving transitions between the m_F states with two different frequencies $\omega_{-1,0}$ and $\omega_{0,+1}$ set to the $m_F = -1 \rightarrow m_F = 0$ and $m_F = 0 \rightarrow m_F = 1$ transitions. By performing independent RWAs with respect to each of these transitions we found that the system could be described by a magnetic Hamiltonian

$$\hat{H} = \frac{\hbar k^2}{2m} + \mathbf{\Omega}(x) \cdot \hat{\mathbf{F}} + \Omega_2 \hat{F}_{zz}^{(2)} \quad (3.42)$$

with $\mathbf{\Omega}_1(x)/\Omega_1 = \cos(2k_R x)\mathbf{e}_x - \sin(2k_R x)\mathbf{e}_y$, $\hat{F}_{zz}^{(2)}\hbar = \hat{F}_z^2/\hbar^2 - 2/3$ is an element of the quadrupole tensor and $\Omega_2 = (\omega_{-1,0} - \omega_{0,1})/2$ can be interpreted as an effective quadratic Zeeman shift. The competing contributions between kinetic and magnetic ordering energies gave rise to different magnetic phases. Figure 7a. shows the ground branch of the dispersion relation for small $\Omega_1 < 4E_L$ (top) and large $\Omega_1 > 4E_L$ (bottom). As the value of Ω_2 is decreased the magnetization in the system changes as the location of the global minima in the dispersion changes. The experimental parameters Ω_1 and Ω_2 spanned a two-dimensional phase diagram shown in Figure 3.42b that we experimentally mapped. The eigenenergies of Equation 7 are plotted in Figure 7c. However in order to get a good agreement between the experiment and the phase diagram we had use the full Floquet Hamiltonian which results in having modified parameters in Equation 3.42 $\Omega_2^{(\text{eff})} = \Omega_2 + \mathcal{O}(\Omega_1^2/\epsilon)$ (red dotted line in Figure 7b). Figure 7d shows three manifolds of Floquet quasienergies for this system, illustrating their periodic nature.

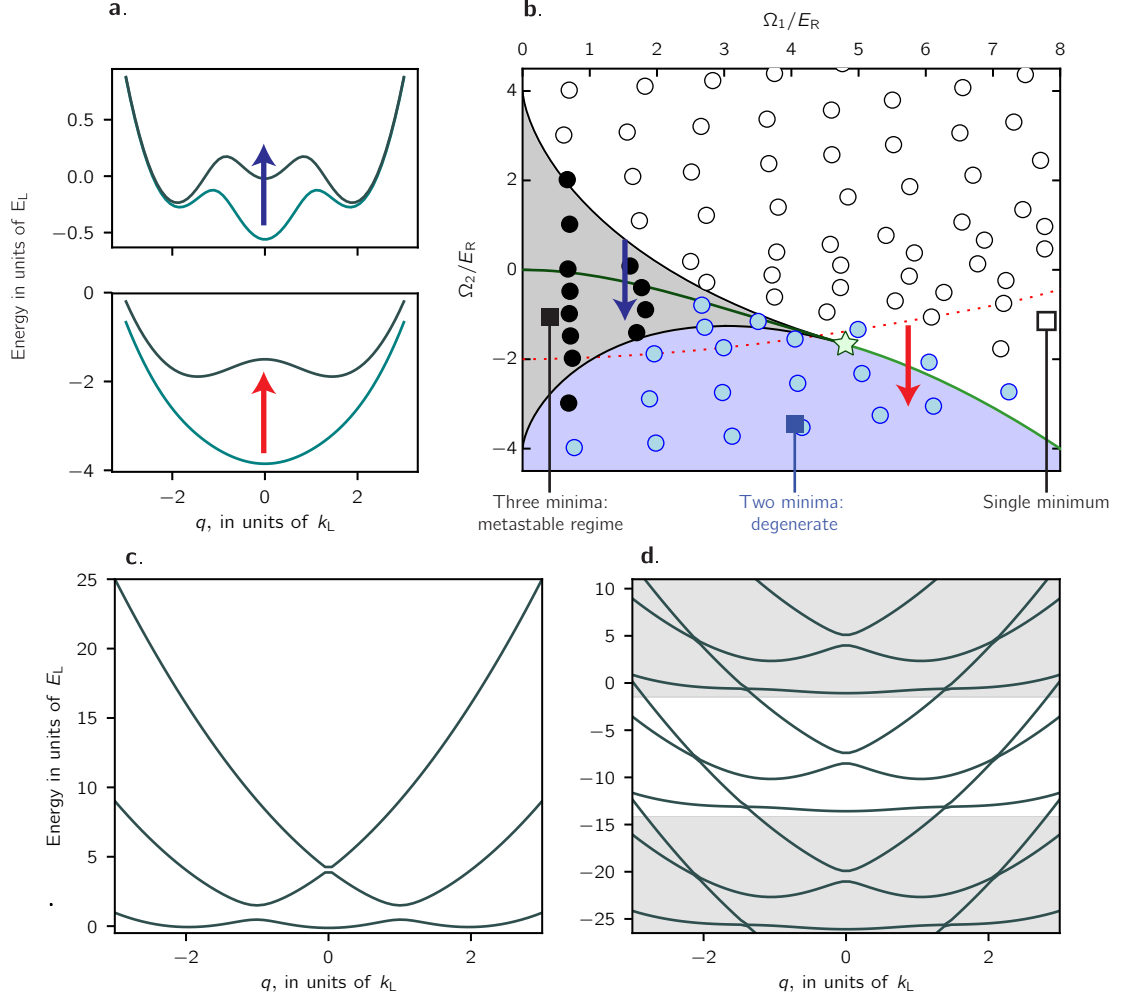


Figure 7: Magnetic phases of a spin-1 SOC system. **a.** Ground state energies of a spin-1 SOC system for $\Omega_1 = 1.5 E_L$ (top) and $\Omega_2 = 1.5 E_L$ (bottom). By changing Ω_2 we moved the location of the central minima. **b.** Phase diagram of a spin-1 SOC system. The green line corresponds to a line of phase transitions where the system goes from magnetized to unmagnetized. **c.** Dispersion relation computed for $\Omega_1 = 2 E_L$, $\Omega_2 = 0$. **d.** Floquet quasienergy dispersion relation for the same parameters. The magnitude of Ω_1 effectively modifies Ω_2 in the RWA Hamiltonian.

3.5 Detection: Resonant absorption imaging

Ultracold atom experiments rely on optical imaging as the main method to probe and characterize the system. In our lab we use resonant absorption imaging which uses a resonant probing laser that is shone at the atomic cloud and then imaged into a charged-coupled device (CCD) camera. From the absorption of the light we can then infer properties about the atoms such as number of atoms, temperature, integrated column density and momentum distribution if we allow the clouds

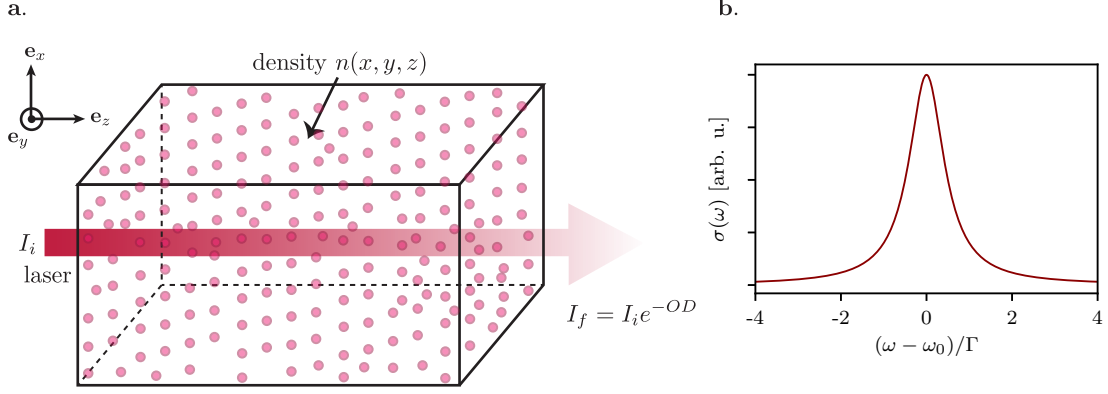


Figure 8: **a.** A laser beam traveling along \mathbf{e}_z through a medium with density $n(x, y, z)$. The intensity decays exponentially with the integrated column density and the scattering cross section $\sigma\omega$. **b.** The scattering cross section has a Lorentzian line shape with a full width half maximum equal to Γ . [TODO: add real data on panel b if I have time.]

to expand.

Consider a laser beam with intensity $I(x, y, z)$ and angular frequency ω propagating along \mathbf{e}_z through a cloud of atoms with density $n(x, y, z)$ as is shown in Figure 8a. We define a (frequency dependent) scattering cross section $\sigma(\omega)$ which characterized the probability of an atom absorbing a probe photon and is given by the Lorentzian function

$$\sigma(\omega) = 3A_{eg} \frac{\pi^2 c^2}{\omega_0^2} \frac{1}{2\pi} \frac{\Gamma}{\delta^2 + \Gamma^2/4} \quad (3.43)$$

plotted in Figure 8b, where Γ is the scattering rate, ω_0 is the transition frequency, $\delta = \omega - \omega_0$ is the detuning and A_{eg} is the Einstein coefficient associated to spontaneous emission. As the beam travels through the cloud it will be absorbed and its intensity is reduced at a rate given by

$$\frac{dI}{dz}(x, y, z) = -n(x, y, z)\sigma(\omega)I(x, y, z). \quad (3.44)$$

In the limit of small intensities we can integrate this expression over the thickness of the cloud and find that the intensity decays exponentially with the density and the scattering cross section

$$I(x, y, z) = I(x, y, 0)e^{-\int_0^z n(x, y, z')\sigma(\omega)dz'}, \quad (3.45)$$

where $\text{OD} = \int_0^z n(x, y, z')\sigma(\omega)dz'$ is the optical depth (OD) of the medium. If

we measure the OD of the cloud it is then straightforward to obtain the integrated column density $n(x, y)$. This result, known as the Beer-Lambert law, works well when using low intensity beams.

In the experiment we measure the optical depth of a cloud by imaging the probe into a CCD camera under two different conditions: first in the presence of atoms to measure the attenuated intensity $I_f = I(x, y, z)$ and then without any atoms to get a measure of the initial intensity $I_i = I(x, y, 0)$. The optical depth can then be computed as

$$OD = \ln \left(\frac{I_f}{I_i} \right). \quad (3.46)$$

Figure 9 show the different images used to compute the OD. In practice we take a third image of the background intensity I_{bg} and subtract it from the other two images.

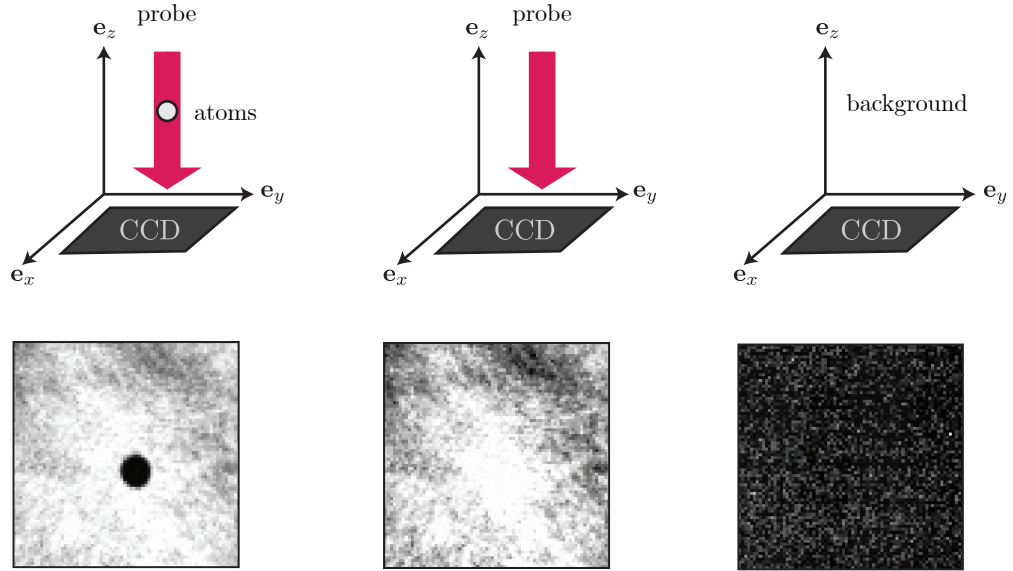


Figure 9: Resonant absorption imaging. An atomic sample is illuminated with a resonant probe whose intensity is later recorded on a CCD camera. Two additional images of the unabsorbed probe intensity and the background intensity are captured in order to reconstruct the optical density of the atoms.

3.5.1 High intensity absorption imaging

The use of the OD to infer the atomic density works well if we assume that the intensity of the probing laser is low such that the atoms mostly stay in the ground state. However at high intensities a significant fraction of the atoms can become excited and effects such as stimulated emission of light have to be taken into account. As a result of this the scattering cross section gets an additional

dependence on intensity (see [25] for a complete derivation)

$$\sigma(\omega, I) = \sigma(\omega) \frac{1}{1 + I/I_{\text{sat}}}, \quad (3.47)$$

where $I_{\text{sat}} = \pi \hbar c \Gamma / 3 \lambda_0^3$ is the saturation intensity, and when $I = I_{\text{sat}}$ the population in the ground and excited state are equal. Integrating Equation 3.44 using the modified expression for $\sigma(\omega, I)$ gives

$$n(x, y) \sigma(\omega) = -\alpha^* \ln(I_f/I_i) + \frac{I_i - I_f}{I_{\text{sat}}}, \quad (3.48)$$

where I have also added an additional dimensionless parameter α^* which can account for imperfections in the imaging process (see [26]).

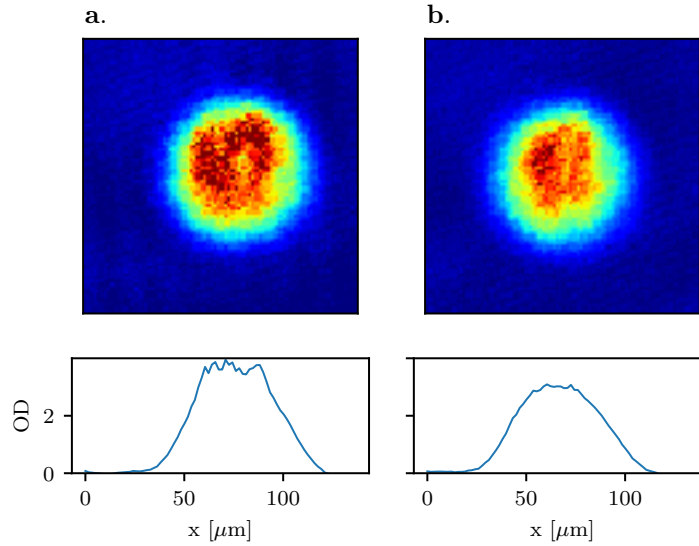


Figure 10: **a.** A BEC imaged at low intensity shows a ‘flat-top’ density profile. **b.** In order to recover the Thomas-Fermi profile it is necessary to image high density BECs with intensities larger than I_{sat} . [TODO: I should try to find better images, this ones don’t look great...]

It is hard reliably measure atomic clouds at low intensity when the OD is of the order of 3 or 4 (such as our BECs) and a significant fraction of the imaging light is absorbed. Due to the limited dynamic range of CCD cameras the measured OD saturates, resulting for example in imaging ‘flat-top’ BECs rather than the usual Thomas-Fermi distribution as shown in Figure 10. To get around this issue we typically image with using intensities $I > I_{\text{sat}}$. In order to correctly compute the column density including saturation effects we need a conversion of I_{sat} from mW/cm^2 to counts per pixel on the CCD camera. We follow the procedure described in [26] find the values of α^* and I_{sat} in counts per pixel. To learn about other effects

such as the recoil momentum from the imaging light that could affect absorption images see [\[27\]](#).